CHANDRA OBSERVATION OF THE PERSISTENT EMISSION FROM THE DIPPING SOURCE XB 1916−053

R. Iaria,[1] T. Di Salvo,[1] G. Lavagetto,[1] N. R. Robba,[1] and L. Burderi[2]

ABSTRACT

We present the results of a 50 ks long *Chandra* observation of the dipping source XB 1916−053. During the observation two X-ray bursts occurred, and the dips were not present at each orbital period. From the zeroth-order image we estimate the precise X-ray coordinates of the source with a 90% uncertainty of $0\farcs6$. In this work we focus on the spectral study of discrete absorption features, during the persistent emission, using the High Energy Transmission Grating Spectrometer on board the *Chandra* satellite. We detect, for the first time in the first-order spectra of XB 1916−053, absorption lines associated with Ne x, Mg xii, Si xiv, and S xvi and confirm the presence of the Fe xxv and Fe xxvi absorption lines with a greater accuracy than the previous *XMM* EPIC pn observation. Assuming that the line widths are due to a bulk motion or a turbulence associated with the coronal activity, we estimate that the lines are produced in a photoionized absorber 4×10^{10} cm from the neutron star , near the disk edge.

Subject headings: line: formation — line: identification — stars: individual (XB 1916−053) — stars: neutron — X-rays: binaries — X-rays: general

Online material: color figures

1. INTRODUCTION

Low-mass X-ray binaries (LMXBs) consist of a low-mass star ($\leq 1\,M_\odot$) and a neutron star (NS), generally with a weak magnetic field ($B \leq 10^{10}$ G). In these systems the X-ray source is powered by the accretion of mass overflowing the Roche lobe of the companion star and forming an accretion disk around the NS. Different inclinations of the line of sight with respect to the orbital plane can explain the different properties of the light curves of these systems. At low inclinations ($i \leq 70°$) eclipses and dips are not observed in the light curves, while they can be present at high inclination angles because the companion star and/or the outer accretion disk intercept the line of sight.

About 10 LMXBs are known to show periodic dips in their X-ray light curves. The dips recur at the orbital period of the system and are probably caused by a thicker region in the outer rim of the accretion disk, formed by the impact with the disk of the gas stream from the companion star (White & Swank 1982). The dip intensities, lengths, and shapes change from source to source and from cycle to cycle. For systems seen almost edge-on, X-ray emission is still visible due to the presence of an extended accretion disk corona (ADC; White & Holt 1982). The ADC can be periodically eclipsed by the companion star and have a radius between 10^9 and 5×10^{10} cm, with an appreciable fraction (from 10% up to 50%) of the accretion disk radius (see Church & Balucinska-Church [2001] for a review). Information on the emitting region in LMXBs can be obtained by studying the spectrum of these high-inclination sources and its evolution during the dips. The energy spectrum of the dipping sources can be well described using two different scenarios. In the "absorbed plus unabsorbed" scenario (e.g., Parmar et al. 1986) the persistent (nondipping) spectral shape was used to model the spectra during the dips but is divided into two parts. One part is allowed to be absorbed, whereas the other one is not. The spectral evolution during dipping is well modeled by a large increase in the

column density of the absorbed component and a decrease of the normalization of the unabsorbed component. The latter component is generally attributed to electron scattering in the absorber. In the "progressive covering" scenario (e.g., Church & Balucinska-Church 1995), the X-ray emission is assumed to originate from a pointlike blackbody, or disk-blackbody component (probably from the NS surface or the inner region of the accretion disk), together with a power law (probably from the extended ADC). These two components can be used to fit the spectrum both during the persistent emission and the dipping activity. Moreover, during the dipping the model well describes the spectral changes due to the partial and progressive covering of the power-law emission from an extended source. The absorption of the pointlike component is allowed to vary independently from that of the extended component, and usually no partial covering is included because during the dipping activity it is fully covered. Both these approaches have been applied to XB 1916−053 (e.g., Yoshida et al. 1995; Church et al. 1997, respectively).

The improved sensitivity and spectral resolution of *Chandra* and *XMM-Newton* allow one to observe narrow absorption features from highly ionized ions (H-like and He-like), in a larger and larger number of X-ray binaries. These features were detected from the microquasars GRO J1655−40 (Ueda et al. 1998; Yamaoka et al. 2001) and GRS 1915+105 (Kotani et al. 2000; Lee et al. 2002). Recently the *Chandra* High-Energy Transmission Grating Spectrometer (HETGS) observations of the black hole candidate H1743−322 (Miller et al. 2004) have revealed the presence of blueshifted Fe xxv and Fe xxvi absorption features suggesting the presence of a highly ionized outflow. All LMXBs that exhibit narrow X-ray absorption features are all known dipping sources (see Table 5 of Boirin et al. 2004) except for GX 13+1. This source shows deep blueshifted Fe absorption features in its HETGS spectrum, again indicative of outflowing material (Ueda et al. 2004).

More recently Díaz Trigo et al. (2006) has modeled the changes in both the X-ray continuum and the Fe absorption features during dipping of six bright LMXBs observed by *XMM*. They concluded that the dips are produced by an increase in the column density and a decrease in the ionization state of the highly ionized absorber.

[1] Dipartimento di Scienze Fisiche ed Astronomiche, Università di Palermo, via Archirafi 36, 90123 Palermo, Italy; iaria@fisica.unipa.it.
[2] Università degli Studi di Cagliari, Dipartimento di Fisica, SP Monserrato-Sestu, KM 0.7, 09042 Monserrato, Italy.

Moreover, outside of the dips, the absorption-line properties do not vary strongly with orbital phase; this implies that the ionized plasma has a cylindrical geometry with a maximum column density close to the plane of the accretion disk. Since dipping sources are normal LMXBs viewed from close to the orbital plane, this implies that ionized plasmas are a common feature of LMXBs. Similar results were obtained by Boirin et al. (2005) studying a *XMM* observation of XB 1323−619.

XB 1916−053 (4U 1916−05) is a dipping source with the shortest period of all dipping sources of 50 minutes (Walter et al. 1982), and it is also notable because of the difference of 1% between the X-ray and optical periods (see Callanan et al. 1995 and references therein). Recently Retter et al. (2002) have favored the superhump model to explain this discrepancy. The superhump model invokes a precessing accretion disk, which identifies the X-ray period as orbital. XB 1916−053 was observed with *Orbiting Solar Observatory 8* (*OSO-8*) and *Ginga* above 10 keV. From the *OSO-8* results of White & Swank (1982) it was clear that dipping persisted up to 20 keV. Using *BeppoSAX* data, Church et al. (1998) showed that the spectrum of the dipping source extends above 100 keV.

Boirin et al. (2004) studied a 17 ks *XMM* observation using European Photon Imaging Camera (EPIC) pn and Reflection Grating Spectrometer (RGS) data in timing mode; the exposure time during the persistent emission was 10 ks. The authors detected, in the EPIC pn data, a Fe xxv Kα and a Fe xxvi Kα absorption line centered at 6.65 and 6.95 keV, with upper limits on the line widths of 100 and 140 eV, respectively; moreover, they marginally detected, in the RGS data between 0.5 and 2 keV, an absorption line centered at 1.48 keV with an upper limit of the corresponding line width of 41 eV and, finally, an absorption edge at 0.99 keV. The absorption line of 1.48 keV was associated with Mg xii Kα, and the absorption edge was associated with moderately ionized Ne and/or Fe. Using the ratio between the Fe xxv and Fe xxvi column density, they have estimated a ionization parameter log (ξ) of 3.92 ergs cm s^{-1}. From a combined analysis during and out of the dipping intervals they concluded that during the dipping activity the absorber is composed of cooler material.

In this work we present a spectral analysis of the persistent emission from XB 1916−053 in the 0.8–10 keV energy range using a 50 ks long *Chandra* observation. The observation covered entirely 16 orbital periods; however, we noted that the dips were not present at all of them. We clearly detected, for the first time in the spectra of this source, the presence of the Ne x Kα, Mg xii Kα, Si xiv Kα, and S xvi Kα absorption lines and confirmed the presence of the Fe xxv Kα and Fe xxvi Kα absorption lines, although the better energy resolution of *Chandra* and the larger statistics allowed us to determine well the widths of each line. We find that the absorption lines were produced in a photoionized absorber placed at the edge of the accretion disk, probably the same absorber producing the dips when it is less photoionized.

2. OBSERVATION

XB 1916−053 was observed with the *Chandra* observatory on 2004 August 7 from 02:27:22 to 16:07:31 UT using the HETGS. The observation had a total integration time of 50 ks and was performed in timed graded mode. The HETGS consists of two types of transmission gratings, the Medium Energy Grating (MEG) and the High Energy Grating (HEG). The HETGS provides high-resolution spectroscopy from 1.2 to 31 Å (0.4–10 keV) with a peak spectral resolution of $\lambda/\Delta\lambda \sim 1000$ at 12 Å for HEG first order. The dispersed spectra were recorded with an array of six charge-coupled devices (CCDs) that are part of the Advanced CCD Imaging Spectrometer-S (ACIS-S; Garmire

et al. 2003).[3] We processed the event list using available software (FTOOLS ver. 6.0.2 and CIAO ver. 3.2 packages) and computed aspect-corrected exposure maps for each spectrum, allowing us to correct for effects from the effective area of the CCD spectrometer.

The brightness of the source required additional efforts to mitigate "photon pileup" effects. A 512 row "subarray" (with the first row = 1) was applied during the observation reducing the CCD frame time to 1.7 s. Pileup distorts the count spectrum because detected events overlap and their deposited charges are collected into single, apparently more energetic, events. Moreover, many events ($\sim$90%) are lost as the grades of the piled up events overlap those of highly energetic background particles and are thus rejected by the onboard software. We, therefore, ignored the zeroth-order events in our spectral analysis. On the other hand, the grating spectra were not, or only moderately (less than 10%), affected by pileup. In this work we analyzed the first-order HEG and MEG spectra; since a 512 row subarray was applied the first-order HEG and MEG energy ranges were shrinked to 1–10 and 0.8–7 keV, respectively.

To determine the zero-point position in the image as precisely as possible, we estimated the mean crossing point of the zeroth-order readout trace and the tracks of the dispersed HEG and MEG arms. We obtained the following coordinates: R.A. = $19^h18^m47\overset{s}{.}871$, decl. = $-05°14'17\overset{''}{.}09$ (J2000.0, with a 90% uncertainty circle of the absolute position of $0\overset{''}{.}6$).[4] We compared the *Chandra* position of XB 1916−053 referred to B1950.0 to the coordinates of the optical counterpart previously reported (Liu et al. 2001 and references therein), finding an angular separation of $8\overset{''}{.}7$. Moreover, we considered the coordinates of XB 1916−053 reported by the NASA HEASARC tool "Coordinate Converter"[5] and compared those to the *Chandra* position achieved by us. The coordinates obtained with the tool were R.A. = $19^h18^m47\overset{s}{.}78$, decl. = $-05°14'11\overset{''}{.}2$ (referred to J2000.0), having an angular separation from the *Chandra* coordinates of $6''$. Unfortunately a comparison with the previous *XMM* observation was not possible because, in that case, the data of XB 1916−053 were taken by all the EPIC cameras in timing mode (see Boirin et al. 2004). In Figure 1 we show a region of sky around the *Chandra* zeroth-order image of XB 1916−053 using the coordinate system referred to B1950.0 in order to compare with the *Chandra* position, the Coordinate Converter tool position, and the optical counterpart position (Liu et al. 2001).

In Figure 2 we showed the 20 s bin time light curve, taking into account only the events in the positive first-order HEG. The mean count rate in the persistent state was 6 counts s^{-1}. During the observation two bursts were observed; the count rate at their peaks was a factor of 3 larger than that during the persistent emission. Moreover, we observed only four dips (see Fig. 2) that did not show a regular periodicity as observed in the previous *XMM* observation (Boirin et al. 2004); in fact, while the second observed dip occurred $\sim$50 minutes after the first one, as expected for this source, the other dips occurred after temporal intervals 2 times larger ($\sim$1.7 hr), indicating that the central region of XB 1916−053 was not occulted at every orbital passage.

3. SPECTRAL ANALYSIS
OF THE PERSISTENT EMISSION

We selected the first-order spectra from the HETGS data, excluding the bursts and the dips, with a total exposure time of the

---

[3] See http://asc.harvard.edu/cdo/about_chandra/ for more details.
[4] See http://cxc.harvard.edu/cal/ASPECT/celmon/ for more details.
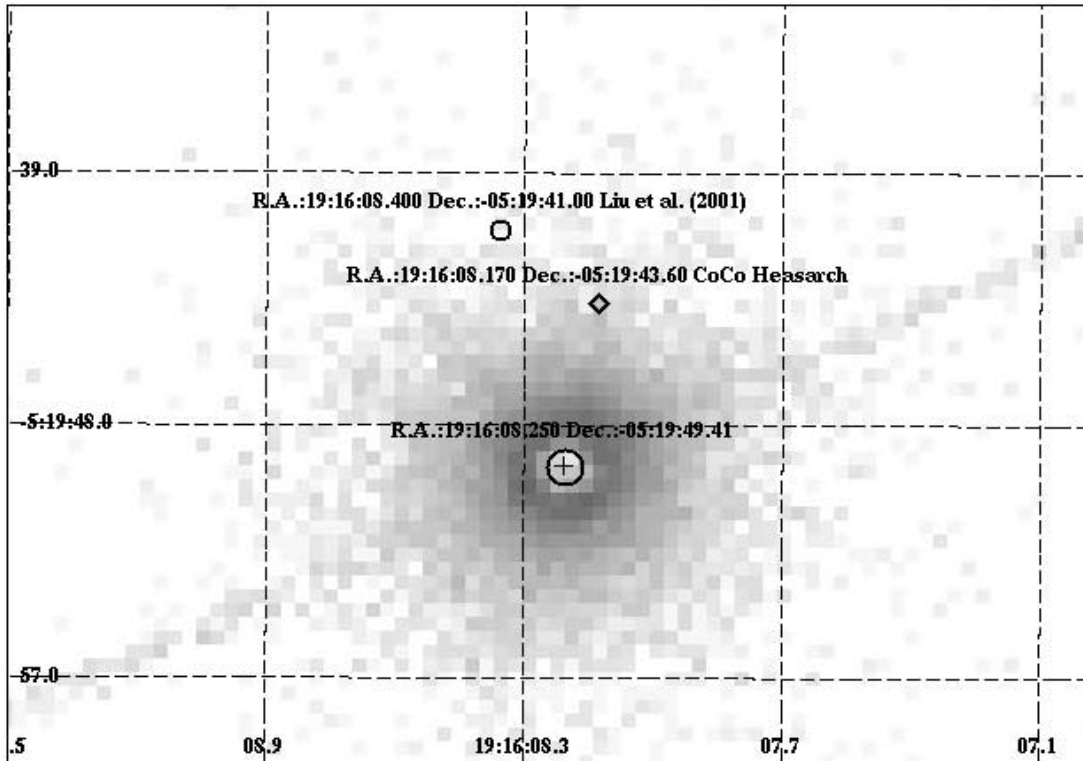[5] See http://heasarc.gsfc.nasa.gov/cgi-bin/Tools/convcoord/convcoord.pl.

FIG. 1.—Region of sky around the *Chandra* zeroth-order image of XB 1916−053. The coordinate system is referred to B1950.0. The circle centered on the best estimation (*plus sign*) of the *Chandra* position has a radius of 0″6. The diamond indicates the position of XB 1916−053 (B1950.0) reported by the HEASARC Coordinate Converter tool (see text); the circle indicates the position of the optical counterpart of XB 1916−053 (B1950.0) reported by Liu et al. (2001). The angular separation between the *Chandra* position and the position reported by the Coordinate Converter tool is 6″.

persistent emission of 42.3 ks. Data were extracted from regions around the grating arms; to avoid overlapping between HEG and MEG data, we used a region size of 25 and 33 pixels for the HEG and MEG, respectively, along the cross-dispersion direction. The background spectra were computed, as usual, by extracting data
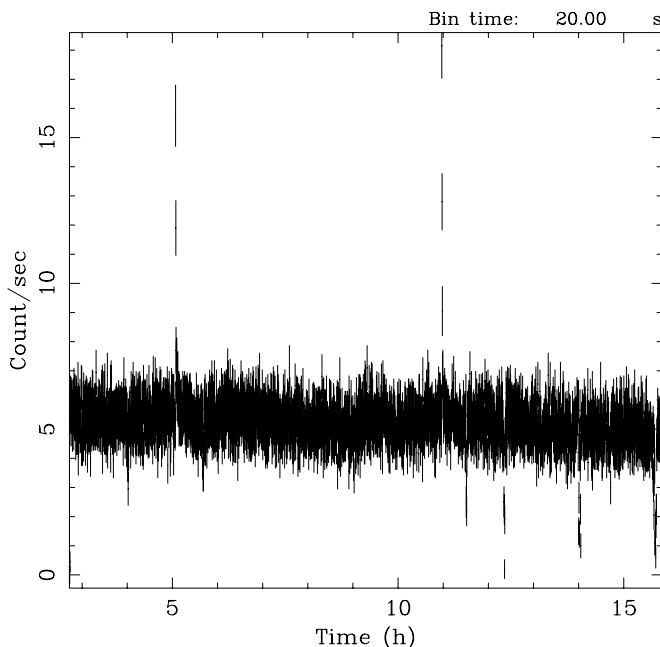

FIG. 2.—The 50 ks light curve of XB 1916−053. During the observation two bursts and four dips were observed. The events used correspond to the positive first-order HEG. The bin time is 20 s.

above and below the dispersed flux. The contribution from the background is 0.4% of the total count rate. We used the standard CIAO tools to create detector response files (Davis 2001) for the HEG−1 (MEG−1) and HEG+1 (MEG+1) order (background-subtracted) spectra. After verifying that the negative and positive orders were compatible with each other in the whole energy range, we co-added them using the script `add_grating_spectra` in the CIAO software, obtaining the first-order MEG spectrum and the first-order HEG spectrum. Finally, we rebinned the resulting first-order MEG and first-order HEG spectra to 0.015 and 0.0075 Å, respectively. It is worth noting that the absolute wavelength accuracy, connected to the error of 0″6 associated with the absolute source position, is ±0.006 and ±0.011 Å for HEG and MEG, respectively.

To fit the continuum, we used the rebinned spectra in the 0.8–7 and 1–10 keV ranges for first-order MEG and first-order HEG, respectively. We fitted the continuum well using an absorbed power law and adding, in the MEG data, a systematic edge at around 2.07 keV with a negative optical depth of ~ -0.2 to take account of an instrumental artifact (see Miller et al. 2002 and references therein). We obtained a χ^2 (dof) of 2325(2395). We found an equivalent hydrogen column of $N_{\rm H} = 0.44 \times 10^{22}$ cm^{-2}, a photon index of 1.5, and a power-law normalization of 0.11. In Figure 3 we reported the data and the residuals with respect to the continuum described above. The presence of several absorption features was clearly evident in the residuals. The corresponding absorbed flux and the unabsorbed luminosity assuming a distance to the source of 9.3 kpc were, respectively, $\sim 7.3 \times 10^{-10}$ ergs cm^{-2} s^{-1} and $\sim 7.5 \times 10^{36}$ ergs s^{-1} in the 0.6–10 keV range. We noted that the luminosity was a factor of 1.7 larger than during the *XMM* observation (see Table 1 in Boirin et al. 2004). To confirm this result, we analyzed the *Rossi X-Ray Timing*
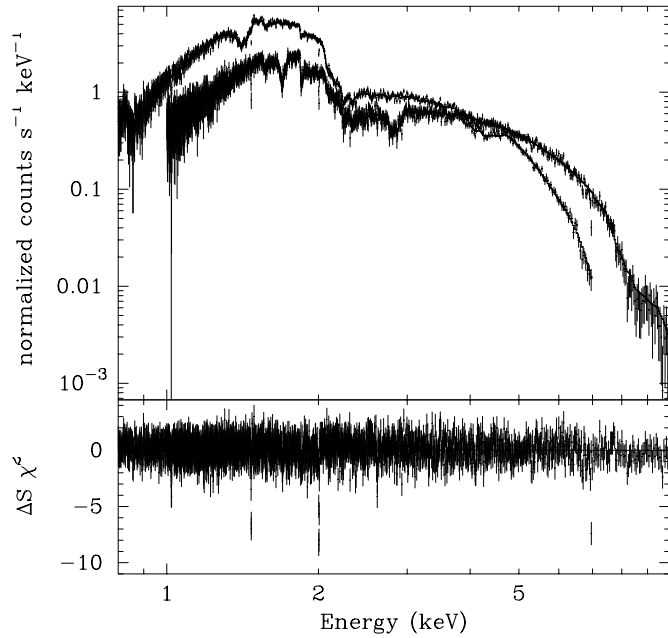
FIG. 3.—Data and residuals of the persistent emission in the energy range 0.8–10 keV for the rebinned first-order MEG and HEG spectra (see text). The continuum is fitted by an absorbed power law. Five absorption features are clearly evident at 1, 1.5, 2, 2.5, and 7 keV, respectively.
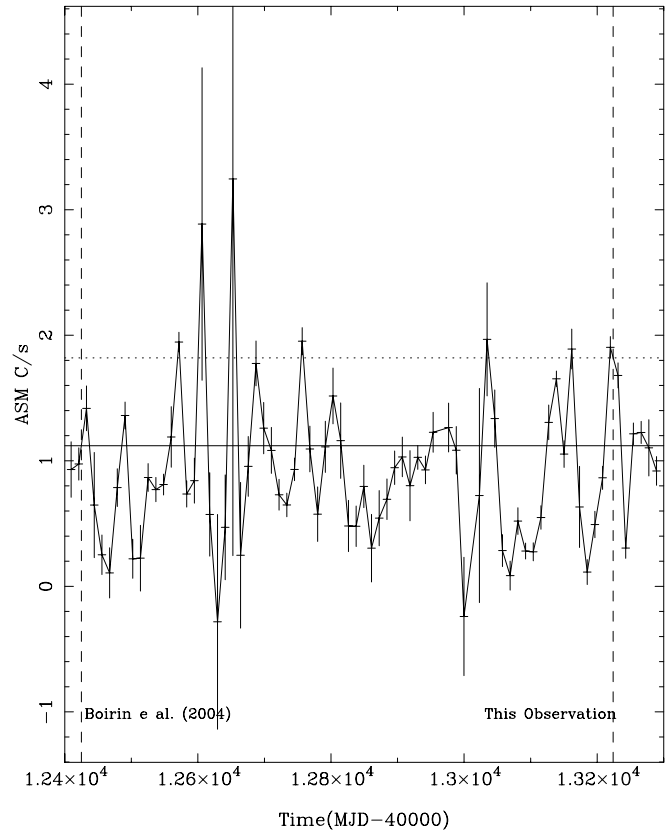

FIG. 4.—*RXTE* ASM light curve of XB 1916−053. The dashed vertical lines indicate the start time of the previous *XMM* observation and of this observation. During the *XMM* observation the ASM count rate was 1.12 counts s^{-1} (*solid horizontal line*); during this observation the ASM count rate was 1.82 counts s^{-1} (*dotted horizontal line*).

Explorer (*RXTE*) All-Sky Monitor (*ASM*) light curve. We observed that during the *XMM* observation the ASM count rate was 1.12 counts s^{-1}, while during the *Chandra* observation the ASM count rate was 1.82 counts s^{-1} with an increase of intensity of almost 1.63, similar to the value obtained from the spectral analysis. In Figure 4 we reported the ASM light curve of XB 1916−053. The dashed vertical lines indicated the start time of the *XMM* and *Chandra* observations; the solid horizontal line indicated the level of the ASM count rate during the *XMM* observation; and, finally, the dotted horizontal line indicated the level of the ASM count rate during the *Chandra* observation.

To resolve the absorption features, we fixed the continuum and added a Gaussian line with negative normalization for each feature. We used the first-order MEG spectrum to resolve the absorption features below 3 keV and the first-order HEG spectrum to resolve those in the 6–7 keV energy band. We detected four absorption lines below 3 keV. These were centered at 1.021, 1.471, 2.004, and 2.617 keV and corresponded to Ne x Kα, Mg xii Kα, Si xiv Kα, and S xvi Kα, respectively; the equivalent widths were −2.13, −1.18, −2.82, and −3.56 eV, respectively. In Figure 5 we showed four expanded views of the residuals with respect to the continuum in the narrow energy ranges around the centroids of each of the absorbed features. In the 6–7 keV energy range we detected two absorption lines centered at 6.693 and 6.966 keV, corresponding to Fe xxv Kα and Fe xxvi Kα, respectively; the equivalent widths were −12.7 and −29.9 eV. In Figure 6 we showed the residuals with respect to the continuum in the 6.4–7.1 keV energy range, and in Table 1 we reported the parameters of the continuum and of each line. We noted that the line energies did not fit with the lab energies. This was not due to a physical effect but to a systematic error associated with the uncertainty of 0″.6 of the source position, which also identifies the zero point of the dispersion arms. Considering the systematic error associated with the absolute wavelength accuracy (i.e., ±0.006 and ±0.011 Å for HEG and MEG, respectively), the line energies are compatible with the lab energies.

4. DISCUSSION

We have analyzed a 42 ks *Chandra* observation of the persistent emission from XB 1916−053. The position of the zeroth-order image of the source provides improved X-ray coordinates for XB 1916−053 (R.A. = 19^{h}18^{m}47^s.871, decl. = −05°14′17″.09), with an angular separation of 8″.7 from the optical counterpart (see Liu et al. 2001) and of 6″ from the X-ray position reported by the Coordinate Converter tool (see § 2). We performed a spectral analysis of the persistent emission using the first-order MEG and HEG spectra. The continuum emission is well fitted by an absorbed power law with photon index 1.5. The equivalent hydrogen column density of the absorbing matter was 0.44 × 10^{22} cm^{-2}; this value is the same obtained by Boirin et al. (2004) in analyzing the *XMM* RGS spectra of XB 1916−053. Also we note that the unabsorbed luminosity, in the 0.6–10 keV energy range, is a factor 1.7 larger than the previous *XMM* observation, this conclusion was further supported by our analysis of the *RXTE* ASM light curve. Another interesting detection is that the dips are not observed at each orbital period; this could be explained by considering that the larger flux from the source during our observation could photoionize more of the matter of the absorber at the disk edge.

We clearly detected the presence of the Ne x (H-like), Mg xii (H-like), Si xiv (H-like), S xvi (H-like), Fe xxv (He-like), and Fe xxvi (H-like) absorption lines. The Fe xxv and Fe xxvi absorption lines were already observed by Boirin et al. (2004) using the *XMM* EPIC pn observation; in that case the line widths had upper limits of <100 and <140 eV, respectively. Thanks to the higher spectral resolution of *Chandra* HEG, to an observation
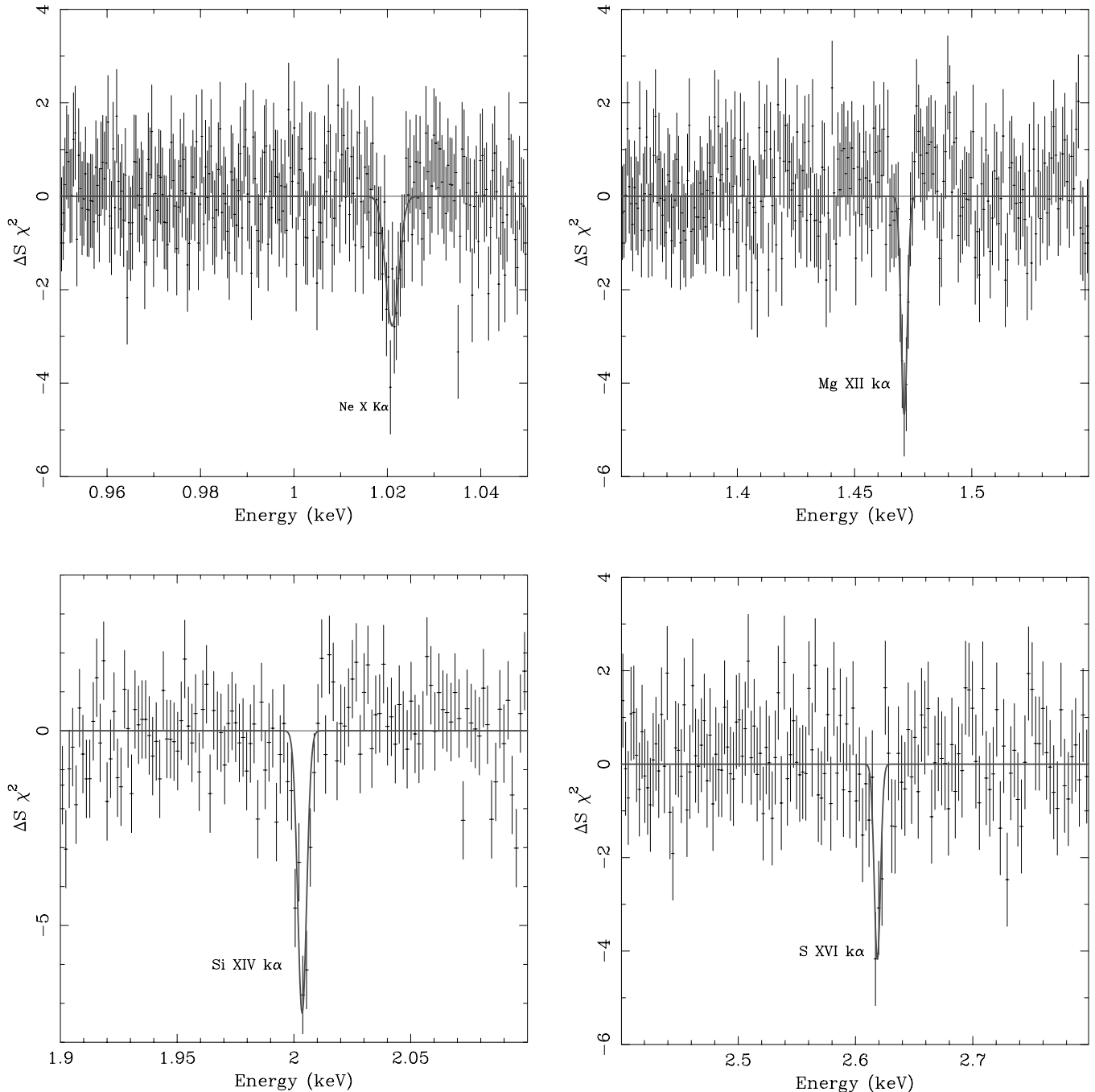
Fig. 5.—Residuals of the first-order MEG spectrum with respect to the best-fit model of the continuum reported in Table 1. In the four panels the residuals are plotted in the energy intervals around the observed absorption features that were identified as Ne x Kα (*top left*), Mg xii Kα (*top right*), Si xiv Kα (*bottom left*), and S xvi Kα (*bottom right*). [*See the electronic edition of the Journal for a color version of this figure.*]

4 times longer and to a source brightness 2 times larger, we found that the line widths are <13 and between 0.1 and 21 eV for Fe xxv and Fe xxvi, respectively. Moreover, Boirin et al. (2004) marginally detected, in the RGS data, a Mg xii absorption line with an upper limit on the line width of 41 eV. Also in this case, thanks to larger statistics, we found a more stringent upper limit on the line width of 1.3 eV. Furthermore, we noted that Boirin et al. (2004) detected in the RGS spectra an absorption edge at 0.99 ± 0.02 keV during the persistent emission of the source. The larger statistics of our observation allowed us to fit well the absorption edge near 1 keV using an absorption line at 1.02 keV associated with Ne x. Finally, we noted that the

energy of the absorption edge was between 0.87 and 0.97 keV in the dipping energy spectra of XB 1916−053 observed with *XMM* RGS (Boirin et al. 2004). We think that this discrete feature could be an absorption line associated with Ne ix. This possibility does not change the scenario proposed by Boirin et al. (2004), who suggested that during the dips the absorbing matter is less photoionized.

Since both Fe xxv and Fe xxvi absorption features were detected, some physical parameters of the plasma responsible for the lines could be estimated. The column density of each ion could be estimated from the equivalent width of the corresponding absorption line, using the relation quoted, for example, by Lee et al.
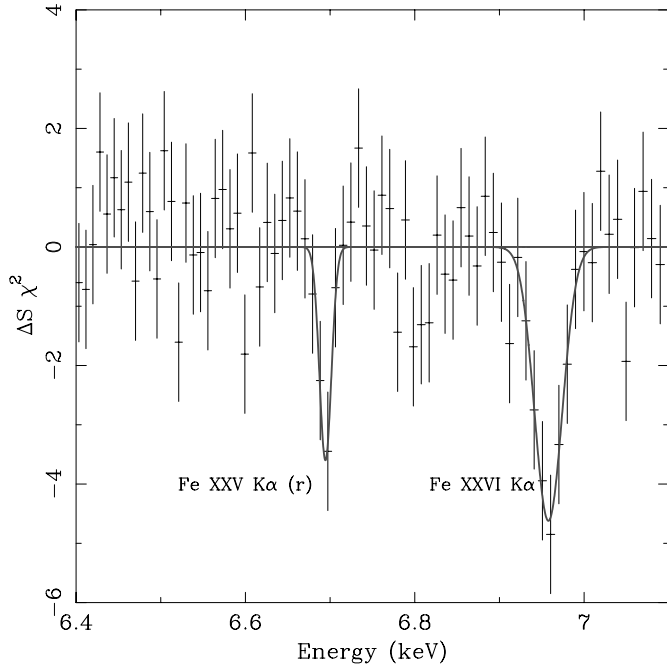
Fig. 6.—Residuals of the first-order HEG spectrum, in the 6.4–7.1 keV energy range, with respect to the best-fit model of the continuum reported in Table 1. Two absorption features, identified as Fe XXV Kα and Fe XXVI Kα, are clearly observed. [*See the electronic edition of the Journal for a color version of this figure.*]

(2002 and references therein) linking the two quantities, which is valid if the line is unsaturated and on the linear part of the curve of growth, which was verified in the case of XB 1916−053. The ratio between Fe XXV and Fe XXVI column densities could then be used to estimate the photoionization parameter, ξ, using the calculations of Kallman & Bautista (2001). Following this approach, we derived column densities of 1.5×10^{17} and 6.6×10^{17} cm^{-2} for Fe XXV and Fe XXVI, respectively. We found $\xi \sim 10^{4.15}$ ergs cm s^{-1}, which was slightly larger than the ionization parameter obtained from *XMM* data by Boirin et al. (2004) of $\xi_{XMM} = 10^{3.92}$ ergs cm s^{-1}. We noted that ξ was a factor of 1.7 larger than ξ_{XMM}, the same factor obtained comparing the unabsorbed luminosity during our observation and the *XMM* observation (see above). Moreover the ionization parameter associated with the H-like ions of Ne, Mg, Si, and S should be $\sim 10^3$, which was lower than that associated with the Fe XXV and Fe XXVI absorption lines. It is worth noting that both we and Boirin et al. (2004) inferred the ionization parameters ξ based on the photoionized model by Kallman & Bautista (2001), which assumed an ionization continuum consisting of a power law with $\Gamma = 1$, but Díaz Trigo et al. (2006) have found a lower value of the ionization parameter of $\log(\xi) = 3.05 \pm 0.04$, using a photon index of $\Gamma = 1.87$ (obtained by fitting the *XMM* data) and assuming a cutoff energy of 80 keV as obtained by Church et al. (1998) using *BeppoSAX* data.

We computed the FWHMs of the absorptions lines in units of kilometers per second; these values were reported in Table 1 and were plotted in Figure 7 in which we note that the values of the FWHMs are compatible with a velocity of 650 km s^{-1} (*dashed horizontal line*). We investigated the nature of the line widths. Initially we assumed that the line widths were produced by thermal broadening, and we estimated the plasma temperature using the relation $kT = 511 m_I/m_e (\sigma/E)^2$ keV, where kT is the temperature of the plasma; m_I and m_e are the mass of the ion and electron, respectively; and σ and E are the width and the centroid of

TABLE 1
RESULTS OF THE SPECTRAL FIT

Parameters	Values
Continuum	
$N_{\rm H}$ (10^{22} cm^{-2})	$0.4448^{+0.0090}_{-0.0087}$
Photon index	$1.4957^{+0.0099}_{-0.0095}$
$N_{\rm po}$	$0.1108^{+0.0014}_{-0.0013}$
Ne X Kα	
E (keV)....................................	$1.02056^{+0.00073}_{-0.00043}$
σ (eV)	$1.40^{+0.71}_{-0.48}$
I (10^{-4} cm^{-2} s^{-1})	$-2.24^{+0.55}_{-0.63}$
EW (eV)	-2.13 ± 0.57
FWHM (km s^{-1})	970^{+490}_{-330}
Mg XII Kα	
E (keV)....................................	$1.47116^{+0.00046}_{-0.00045}$
σ (eV)	<1.3
I (10^{-5} cm^{-2} s^{-1})	$-7.4^{+1.8}_{-2.0}$
EW (eV)	$-1.18^{+0.29}_{-0.32}$
FWHM (km s^{-1})	<620
Si XIV Kα	
E (keV)....................................	$2.00352^{+0.00071}_{-0.00072}$
σ (eV)	$1.79^{+1.03}_{-0.84}$
I (10^{-4} cm^{-2} s^{-1})	$-1.13^{+0.20}_{-0.21}$
EW (eV)	-2.82 ± 0.53
FWHM (km s^{-1})	630^{+360}_{-300}
S XVI Kα	
E (keV)....................................	$2.61653^{+0.00472}_{-0.00082}$
σ (eV)	$2.76^{+158.03}_{-0.28}$
I (10^{-5} cm^{-2} s^{-1})	$-9.6^{+3.6}_{-1.9}$
EW (eV)	$-3.56^{+1.32}_{-0.69}$
FWHM (km s^{-1})	740^{+42000}_{-100}
Fe XXV Kα	
E (keV)....................................	$6.6925^{+0.0088}_{-0.0057}$
σ (eV)	<13
I (10^{-5} cm^{-2} s^{-1})	$-8.3^{+3.7}_{-3.5}$
EW (eV)	-12.7 ± 5.6
FWHM (km s^{-1})	<1400
Fe XXVI Kα	
E (keV)....................................	$6.9558^{+0.0062}_{-0.0066}$
σ (eV)	$9.7^{+21.0}_{-9.6}$
I (10^{-4} cm^{-2} s^{-1})	$-1.83^{+0.46}_{-0.58}$
EW (eV)	$-29.9^{+7.6}_{-9.4}$
FWHM (km s^{-1})	980^{+2100}_{-970}

NOTES.—The model is composed of a power law with absorption from neutral matter. Uncertainties are at the 90% confidence level for a single parameter; upper limits are at the 95% confidence level. The expression $N_{\rm po}$ indicates the normalization of the power-law component in units of photons keV^{-1} s^{-1} cm^{-2} at 1 keV. The parameters of the Gaussian emission lines are E, σ, I, and EW, indicating the centroid in keV, the width in keV, the intensity of the line in units of photons s^{-1} cm^{-2}, and the equivalent width in eV, respectively.
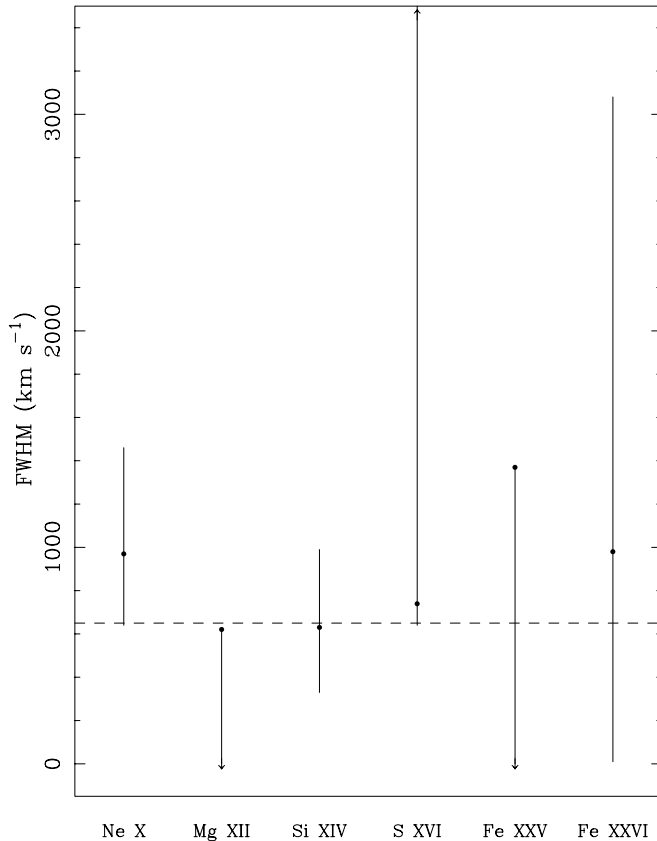
Fig. 7.—FWHM in kilometers per second of the observed absorption lines. All the FWHMs are compatible with a velocity of 650 km s^{-1}, indicated by the dashed horizontal line.

the absorption line in keV, respectively. We found that the Ne x, Mg xii, Si xiv, and S xvi absorption lines should be produced in a region with a temperature between 20 and 40 keV, while we found an upper limit of ∼200 keV for the temperature of the region where the Fe xxv and Fe xxvi absorption line should be produced. The interpretation of the line as thermally broadened was not consistent with the interpretation of the iron line ratios as diagnostics of the ionization parameter. If the temperature was really 20 keV or greater, then all the elements would be fully stripped, with the possible exception of iron. A more probable scenario was that the line widths were broadened by some bulk motion or supersonic turbulence with a velocity around 650 km s^{-1} as indicated by the FWHMs. XB 1916−053 has an extended corona around the compact object (Church et al. 1998). By assuming that the mechanism generating the turbulence or bulk motion was due to the presence of the extended corona, we can obtain some information about where the absorption lines were produced. Coronal models tend to have turbulent velocities that are locally proportional to the virial or rotational velocity (Woods et al. 1996). At 10^9 cm (the coronal radius; see Narita et al. 2003)

the virial velocity is 4400 km s^{-1} for a NS of 1.4 $M_\odot$. It is very difficult to construct plausible dynamic models in which the matter moves at 10% of the virial velocity; these lines should be then produced at much larger distances, nearer to 4×10^{10} cm, i.e., near the disk edge. According to this scenario, we concluded that the absorbing matter was located at the same distance from the NS of the bulge that was likely responsible for the dips themselves. In the hypothesis that the thickness of the absorbing region was much less than 4×10^{10} cm, its distance from the source, we could estimate a constraint on the thickness d of the absorber using $d < L/\xi N$ (Reynolds & Fabian 1995), where L is the unabsorbed luminosity, N is the equivalent hydrogen column density of the photoionized matter, and ξ is the corresponding ionization parameter. Assuming the cosmic abundance for iron and a population of Fe xxv with respect to neutral iron of 0.5, we found $d < 8 \times 10^4$ km.

5. CONCLUSION

We studied the persistent emission of XB 1916−053 using a 42 ks *Chandra* observation. We improved the position of the source; the new coordinates are R.A. = $19^h18^m47^s871$ and decl. = $-05°14'17''09$ (J2000.0) with an uncertainty circle of the absolute position of $0''6$.

We detected the Ne xii, Mg xii, Si xiv, and S xvi absorption lines centered at 1.021, 1.471, 2.004, and 2.617 keV, respectively. These lines were never observed before in XB 1916−053. Of all the X-ray binaries exhibiting absorption lines, only Cir X-1 shows the same wide series of absorption lines, although in that case P Cygni profiles are evident (Brandt & Schulz 2000).

We confirmed the presence of the Fe xxv Lyα and Fe xxvi Lyα absorption lines at 6.69 and 6.96 keV, respectively, already observed by *XMM*. From the study of equivalent widths of the two lines we inferred a ionization parameter log (ξ) of 4.15, which was a factor of 1.7 larger than during the previous *XMM* observation. The unabsorbed luminosity in the 0.6–10 keV energy range, 7.5×10^{36} ergs s^{-1}, was also larger by the same factor, and we verified this result by studying the *RXTE* ASM light curve of XB 1916−053. The increase of the ionization parameter and of the luminosity of the same factor indicated that these two lines were produced in the same region. We estimated that the absorption-line widths could be compatible with a broadening caused by bulk motion or turbulence connected to the coronal activity. We find from the broadening of the absorption lines that these were produced at a distance from the NS of 4×10^{10} cm, i.e., near the disk edge and at the same radius of the absorber that causes the dipping when the corresponding ionization parameter decreases.

REFERENCES

Boirin, L., et al. 2004, A&A, 418, 1061
———. 2005, A&A, 436, 195
Brandt, W. N., & Schulz, N. S. 2000, ApJ, 544, L123
Callanan, P. J., Grindlay, J. E., & Cool, A. M. 1995, PASJ, 47, 153
Church, M. J., & Balucinska-Church, M. 1995, A&A, 300, 441
———. 2001, A&A, 369, 915
Church, M. J., et al. 1997, ApJ, 491, 388
———. 1998, A&A, 338, 556
Davis, J. E. 2001, ApJ, 562, 575
Díaz Trigo, M., et al. 2006, A&A, 445, 179

Garmire, G. P., et al. 2003, Proc. SPIE, 4851, 28
Kallman, T., & Bautista, M. 2001, ApJS, 133, 221
Kotani, T., et al. 2000, ApJ, 539, 413
Lee, J. C., et al. 2002, ApJ, 567, 1102
Liu, Q. Z., van Paradjis, J., & van den Heuvel, E. P. J. 2001, A&A, 368, 1021
Miller, J. M., et al. 2002, ApJ, 578, 348
———. 2004, preprint (astro-ph/0406272)
Narita, T., Grindlay, J. E., & Bloser, P. F. 2003, ApJ, 593, 1007
Parmar, A. N., et al. 1986, ApJ, 308, 199
Retter, A., et al. 2002, MNRAS, 330, L37

Reynolds, C. S., & Fabian, A. C. 1995, MNRAS, 273, 1167
Ueda, Y., et al. 1998, ApJ, 492, 782
———. 2004, ApJ, 609, 325
Walter, F. M., et al. 1982, ApJ, 253, L67
White, N. E., & Holt, S. S. 1982, ApJ, 257, 318

White, N. E., & Swank, J. H. 1982, ApJ, 253, L61
Woods, D. T., et al. 1996, ApJ, 461, 767
Yamaoka, K., et al. 2001, PASJ, 53, 179
Yoshida, K., et al. 1995, PASJ, 47, 141

Note added in proof.—While this paper was in press, we became aware of a paper by Juett & Chakrabarty (ApJ, in press; astro-ph/0604046), based on the same data. The conclusions that these authors draw regarding the origin of the absorption features and their location within the system are different from ours.